Spatiotemporal Variations in Hydroclimate across the Mediterranean Andes (30°–37°S) since the Early Twentieth Century

Spatiotemporal Variations in Hydroclimate across the Mediterranean Andes (30°–37°S) since the Early Twentieth Century

ÁLVARO GONZÁLEZ-REYES,[a] JAMES MCPHEE,[b] DUNCAN A. CHRISTIE,[c] CARLOS LE QUESNE,[d] PAUL SZEJNER,[e] MARIANO H. MASIOKAS,[f] RICARDO VILLALBA,[f] ARIEL A. MUÑOZ,[g] AND SEBASTIÁN CRESPO[f]

[a] *Instituto de Ciencias de la Tierra, Facultad de Ciencias, Universidad Austral de Chile, Valdivia, Chile*
[b] *Departamento de Ingeniería Civil and Advanced Mining Technology Center, Facultad de Ciencias Físicas y Matemáticas, Universidad de Chile, Santiago, Chile*
[c] *Laboratorio de Dendrocronología y Cambio Global, Instituto de Conservación Biodiversidad y Territorio, Facultad de Ciencias Forestales y Recursos Naturales, Universidad Austral de Chile, Valdivia, and Center for Climate and Resilience Research (CR)2, Universidad de Chile, Santiago, Chile*
[d] *Laboratorio de Dendrocronología y Cambio Global, Instituto de Conservación Biodiversidad y Territorio, Facultad de Ciencias Forestales y Recursos Naturales, Universidad Austral de Chile, Valdivia, Chile*
[e] *Laboratory of Tree-Ring Research, and School of Natural Resources and the Environment, The University of Arizona, Tucson, Arizona*
[f] *Instituto Argentino de Nivología, Glaciología y Ciencias Ambientales, CCT CONICET Mendoza, Mendoza, Argentina*
[g] *Instituto de Geografía, Pontificia Universidad Católica de Valparaíso, Valparaíso, Chile*

(Manuscript received 13 January 2016, in final form 10 January 2017)

ABSTRACT

In the Mediterranean Andes region (MA; 30°–37°S), the main rivers are largely fed by melting snowpack and provide freshwater to around 10 million people on both sides of the Andes Mountains. Water resources in the MA are under pressure because of the extensive development of industrial agriculture and mining activities. This pressure is increasing as the region faces one of its worst recorded droughts. Previous studies have pointed to El Niño–Southern Oscillation (ENSO) as the main climatic force impacting the MA. However, the role of decadal and multidecadal climate variability, their spatial patterns, and the recurrence of long-term droughts remains poorly studied. In an attempt to better understand these factors, spatial and temporal patterns of hydroclimatic variability are analyzed using an extensive database of streamflow, precipitation, and snowpack covering the period between 1910 and 2011. These analyses are based on the combination of correlation, principal components, and kernel estimation techniques. Despite a general common pattern across the MA, the results presented here identify two hydroclimatic subregions, located north and south of 34°S. While the interannual variability associated with ENSO is slightly stronger north of 34°S, the variability associated with the Pacific decadal oscillation (PDO) and/or the interdecadal Pacific oscillation (IPO) index shows similar patterns in both regions. However, variations produced by the IPO forcing seem to be greater in the southern subregion since 1975. The estimations presented here on drought recurrence reveal a generalized increase in dry extremes since the 1950s. These findings suggest that the northern MA is more vulnerable to changes in hydrology and climate than the southern MA.

1. Introduction

The Andes is the largest mountain chain in the Southern Hemisphere, acting as a regional ''water tower'' for many South American countries from the tropics to the southern tip of the continent (8°N–55°S). The Mediterranean Andes region (MA; 30°–37°S) is located in the transition between two major macroclimate regions in South America, namely, the subtropical desert Andes to the north and the wet temperate Andes to the south (Lliboutry 1998). Several studies in the region have identified recent environmental changes characterized by 1) an increase of mean air temperature ($+0.25$°C decade^{-1}) during the last three decades (1979–2006; Falvey and Garreaud 2009); 2) a reduction of the area covered by glaciers (Bown et al. 2008; Masiokas et al. 2009); 3) an increase of the 0°C

Corresponding author e-mail: Álvaro González-Reyes, gonzalezreyesalvaro@gmail.com

DOI: 10.1175/JHM-D-16-0004.1

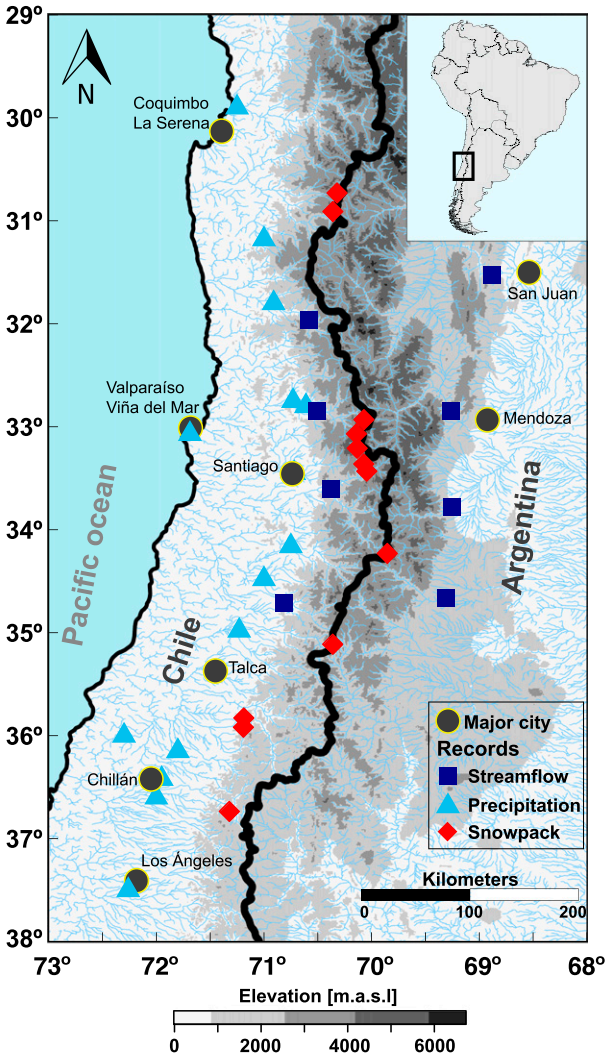

FIG. 1. Study region and spatial distribution of the streamflow, snowpack, and precipitation records across the MA. The main cities are shown as circles. The thick black line indicates the Chilean–Argentinean border across the Andes, which follows the Continental Divide.

isotherm (Carrasco et al. 2008); and 4) a negative, although not significant, precipitation trend since the beginning of the twentieth century (Vuille and Milana 2007; Le Quesne et al. 2009; Quintana and Aceituno 2012). The rivers in the MA provide freshwater to around 10 million people on both sides of the Andes Mountains in Chile and Argentina (Fig. 1). These rivers are fed by precipitation during winter and by the melting of the snowpack in the high mountains during spring and summer (Masiokas et al. 2006).

Large-scale climate forcings, such as El Niño–Southern Oscillation (ENSO), have strong influences over the MA climate. El Niño (La Niña) conditions are usually associated with years of above (below) average winter precipitation (Rutllant and Fuenzalida 1991; Montecinos and Aceituno 2003), abundant (reduced) snowpack accumulation (Masiokas et al. 2006), and a concurrent increase (decrease) in river discharge (Aceituno and Garreaud 1995; Cortés et al. 2011). On the other hand, the positive (negative) phase of the Pacific decadal oscillation (PDO) has been associated with abundant (reduced) precipitation (Garreaud et al. 2009) as well as above (below) average snowpack accumulation and streamflows in the MA (Masiokas et al. 2010).

Since 2010, the MA has been affected by severe and persistent dry episodes, leading to significant water scarcity and subsequent conflicts between economic sectors, the government, and rural communities. In the context of this long-term drought, water deficits have been geographically variable, showing dissimilar year-to-year spatial patterns in central Chile (CR2 2016). In this regard, investigations into the spatial and temporal evolution of droughts in the MA are a high priority, not only to characterize the return intervals of extreme droughts but also to plan future water uses and adaptations to climate change. In addition, this information will help to refine regional climate models. Previous studies have evaluated the spatial return intervals of drought events along the Andes based on precipitation thresholds (Núñez et al. 2011) and drought indices such as the standardized precipitation evapotranspiration index (SPEI) over the 29°–35°S region (Meza 2013). However, joint spatial and temporal drought recurrence analyses based on multiple combinations of hydroclimatic variables such as snowpack, precipitation, and streamflow records have not been previously undertaken.

In this contribution, we analyze and update the high-quality hydroclimatic database for the MA consisting of streamflow, precipitation, and snowpack instrumental records. Based on these observations, we intend to 1) identify the main spatiotemporal patterns modulating the MA hydroclimate; 2) analyze the relationships between the MA hydroclimate patterns and large-scale climate forcings such as ENSO, PDO, and interdecadal Pacific oscillation (IPO) index; and 3) evaluate the recurrence interval of extreme drought events across the MA. Since this region encompasses the transition between the dry Andes of Atacama to the north and the wet Andes of the Valdivian ecoregion to the south, we hypothesize the occurrence of spatial and temporal variations in drought events across the latitudinal moisture gradient in the region.

2. Data and methodology

a. Study region and climate setting

The MA encompasses the central Andes of Argentina and Chile, located between 30° and 37°S and 69° and

72°W (Fig. 1). The adjacent lowlands are highly populated with more than 10 million inhabitants. The Chilean population in the region is over 8.5 million and represents more than 55% of the total national population (INE 2003). On the drier Argentinean slopes of the Andes, mountain rivers provide water to more than 2.4 million people concentrated in the irrigated oases of Mendoza and San Juan (INDEC 2010).

The climate in the central Andes is a Mediterranean-type climate, with more than 70% of annual precipitation occurring during the austral winter (May–August). On the western side of the Andes (Chile), the dry summer season starts in October–November. Almost all moisture comes from westerly Pacific frontal systems precipitating as rainfall in the lowlands and as snow in the mountains (Miller 1976; Aceituno 1988; Garreaud 2009). The orographic rain shadow caused by the Andes, with peaks over 6000 m, reduces the total amount of incident precipitation to the east of the Continental Divide. On the eastern slopes and lowlands of the MA, a well-defined maximum in precipitation occurs during austral summer in connection with the development of the South American monsoon (Vera et al. 2006). The total annual precipitation (1960–2000) at the Los Andes meteorological station in Chile is 269.5 mm, with 77.9% concentrated in winter (May–August), whereas at the Mendoza airport station in Argentina, total annual precipitation is 193.7 mm, with just 17.7% recorded during the winter months. In contrast, spring and summer precipitation (October–March) represents more than 70% of the total annual rainfall recorded at the Mendoza airport.

Despite these differences in precipitation regime on both sides of the Andes, streamflow, which originates from snow and glacier melt in the Andes Mountains, shows a common seasonal regime for both slopes of the Andes (Masiokas et al. 2013), common for energy-driven hydrological systems. As a result, Argentinean and Chilean river flows in the MA show a strong mean intercorrelation over the snowmelt season (mean $r = 0.83$; $P < 0.001$; 1954–2007 period).

b. *Identification of spatiotemporal hydroclimatic patterns*

Spatial and temporal patterns of hydroclimatic variability are based on a network of snowpack, precipitation, and streamflow records located in the MA (Fig. 1; Table 1). The snowpack and streamflow records have been used in previous studies (Masiokas et al. 2006, 2009), where streamflow registers present a low degree of impairment. The MA presents continuous precipitation and streamflow records available since the early twentieth century (e.g., Santiago, Chile, precipitation and Río Mendoza in Argentina), which allow the evaluation of spatiotemporal variations in the hydroclimate with a long-term perspective. To determine the main spatial and temporal modes of streamflow and precipitation of the MA, we performed a principal component analysis (PCA; Wilks 2011) using varimax optimization on each set of hydroclimatic variables (precipitation, streamflow, and snowpack). Streamflow was analyzed using the mean annual river discharges over the July–June hydrological year (i.e., the 1997 hydrological year extends from July 1997 to June 1998) for the 1954–2007 common period. The maximum river discharge by snowmelt occurs during austral spring and austral summer months. PCA was applied to total annual precipitation from January to December considering the 1960–2000 common period between stations. Finally, the selected common period for the maximum value of snowpack in each year for PCA was shorter, spanning the interval 1961–90. Missing values in the snowpack records were filled with the corresponding mean value of each record based on the 1961–90 interval. A summary of the hydroclimatic records used in this work is outlined in Table 1.

Based on the first and second principal component (PC1 and PC2) station loading factors (values ≥ 0.70 and summarized in Table A1 in the appendix), we arrange the records in two subregional hydroclimatic series integrating snowpack, precipitation, and streamflow records. We used the 1961–90 common reference period for snowpack, precipitation, and streamflow stations. For each selected station, data were first expressed as percentage of the mean over the 1961–90 common period and then composited into regional series. Two subregional series (northern and southern subregions) with an annual resolution were identified spanning the 1910–2011 period. Precipitation and streamflow information were used starting with the year 1910, while snowpack information has been added since the year 1959 because of its short instrumental period.

c. *Relationships between regional hydroclimatology and large-scale climate forcings*

To evaluate the interannual-scale and decadal-to-multidecadal-scale relationships between the MA hydroclimate and large-scale climate forcings (ENSO, PDO, and IPO), we computed Pearson correlations between hydroclimatic parameters and the sea surface temperature (SST) from the Niño-3.4 region, the IPO, and the PDO using year-to-year correlations and running blocks. The Niño-3.4 index is based on SST variations over the east-central tropical Pacific at 5°N–5°S,

TABLE 1. Snowpack (Sn), precipitation (Pp), and streamflow Q stations of the MA utilized. The sources are the Chilean Dirección General de Aguas (DGA), the Argentinean Departamento General de Irrigación (DGI), the Chilean Empresa Nacional de Electricidad Sociedad Anónima (ENDESA), Dirección Meteorológica de Chile (DMC), and the Argentinean Subsecretaría de Recursos Hídricos (SSRH).

Station (code)	Lat, lon	Elev (m)	Period	Avg (1961–90)	Data source
Quebrada Larga (QLA; Sn)	30°43′S, 70°22′W	3500	1956–2010	236.6 mm	DGA
Cerro Vega Negra (CVN; Sn)	30°55′S, 70°31′W	3600	1972–2009	583.2 mm	DGA
Portillo (POR; Sn)	32°50′S, 70°07′W	3000	1951–2010	683.8 mm	DGA
Cerro Negro (CNE; Sn)	33°08′S, 70°15′W	3450	1971–90	772.5 mm	DGA
Barros Negros (BNE; Sn)	33°20′S, 70°15′W	3380	1965–90	472.7 mm	DGA
Rodeo Alfaro (RAL; Sn)	33°37′S, 70°18′W	2200	1967–90	385.3 mm	DGA
Laguna Negra (LNE; Sn)	33°40′S, 70°08′W	2768	1965–2010	601.7 mm	DGA
Laguna del Diamante (LDI; Sn)	34°15′S, 69°42′W	3310	1956–2010	467.8 mm	DGI
Valle Hermoso (VHE; Sn)	35°09′S, 70°12′W	2275	1952–2010	820.4 mm	DGI
Calabozo (CSA; Sn)	35°36′S, 71°26′W	1850	1957–97	532 mm	ENDESA
Cerro La Gloria (CLG; Sn)	36°36′S, 71°21′W	1500	1969–97	739.8 mm	DGA
Volcán Chillan (VCH; Sn)	36°50′S, 71°25′W	2400	1966–2010	840.9 mm	DGA
La Serena (LSE; Pp)	29°54′S, 71°15′W	30	1869–2011	79.8 mm	DMC
Combarbalá (COM; Pp)	31°11′S, 71°02′W	900	1922–2011	210.8 mm	DMC
Salamanca (LSE; Pp)	31°48′S, 70°55′W	570	1942–2011	220.5 mm	DMC
San Felipe (SFP; Pp)	32°44′S, 70°43′W	640	1962–2011	206.9 mm	DGA
Los Andes (LAN; Pp)	32°50′S, 70°37′W	815	1907–2011	273 mm	DMC
Valparaíso (VAL; Pp)	33°01′S, 71°38′W	40	1869–2011	371.5 mm	DMC
Santiago-Q.Normal (QUI; Pp)	33°27′S, 70°42′W	520	1866–2011	312.5 mm	DMC
Rancagua (RAN; Pp)	34°10′S, 70°45′W	500	1910–2011	415.5 mm	DMC
San Fernando (SFE; Pp)	34°35′S, 71°00′W	350	1910–2011	700.1 mm	DMC
Cúrico (CUR; Pp)	34°59′S, 71°14′W	100	1907–2011	698 mm	DMC
Cauquenes (CAU; Pp)	35°59′S, 72°22′W	180	1919–2011	642.7 mm	DMC
Parral (PAR; Pp)	36°09′S, 71°50′W	170	1919–2000	942.6 mm	DMC
San Carlos (SCA; Pp)	36°25′S, 71°55′W	172	1919–2003	1000.1 mm	DMC
Chillán (CHL; Pp)	36°34′S, 72°02′W	124	1919–2011	1020.2 mm	DMC
Los Angeles (LAG; Pp)	37°24′S, 72°25′W	120	1918–2006	1070.7 mm	DMC
San Juan-Km. 47.3 (SJU; Q)	31°32′S, 68°53′W	945	1909–2007	60 $m^3 s^{-1}$	SSRH
Choapa-Cuncumén (CHO; Q)	31°58′S, 70°35′W	955	1941–2009	9.8 $m^3 s^{-1}$	DGA
Aconcagua-Chacabuquito (ACO; Q)	32°51′S, 70°31′W	1030	1914–2009	34.3 $m^3 s^{-1}$	DGA
Mendoza-Guido (MNZ; Q)	32°51′S, 69°16′W	1550	1909–2011	46.8 $m^3 s^{-1}$	SSRH
Maipo-El Manzano (MAI; Q)	33°36′S, 70°23′W	890	1947–2011	114.8 $m^3 s^{-1}$	DGA
Tunuyán-Valle de Uco (TUN; Q)	33°47′S, 69°15′W	1200	1954–2008	29.8 $m^3 s^{-1}$	SSRH
Diamante-La Jaula (DIA; Q)	34°40′S, 69°19′W	1500	1938–2008	32.8 $m^3 s^{-1}$	SSRH
Tinguiririca-B. Los Briones (TIN; Q)	34°43′S, 70°49′W	518	1942–2009	50.2 $m^3 s^{-1}$	DGA

170°–120°W and was used as an indicator of ENSO (Trenberth 1997). The IPO index represents the leading mode of long-term SST variability over the Pacific Ocean and captures multidecadal variation of ENSO or ENSO-like interdecadal variability (Zhang et al. 1997; Power et al. 1999). The PDO index is defined as the leading principal component of SST in the Pacific northward of 20°N (Mantua et al. 1997). Sources of these indices are outlined in Table 2. Finally, we used a Mann–Whitney test to evaluate temporal shifts in the mean

TABLE 2. Climate indices used in this study. The data sources are the Institute of Global Environment and Society (IGES), Met Office, NOAA/NCEP/CPC, and Joint Institute for the Study of the Atmosphere and Ocean (JISAO) at the University of Washington.

Climate index description	Period	Data source	Reference
IPO: Interdecadal Pacific oscillation	1871–2007	IGES (http://www.iges.org/c20c/IPO_v2.doc)	Met Office
Niño-3.4: Mean monthly SST anomalies for the Niño-3.4 region, east-central tropical Pacific (5°N–5°S, 170°–120°W)	1866–2011	NOAA/NCEP/CPC (http://www.cpc.ncep.noaa.gov/data/indices/)	Trenberth (1997)
PDO: Leading PC of monthly SST anomalies in the North Pacific Ocean, poleward of 20°N	1900–2011	JISAO (http://jisao.washington.edu/data/pdo)	Mantua et al. (1997)

correlations in order to highlight periods where relationships are statistically significant.

d. Drought recurrence over the last century

Previous studies on the MA have analyzed the influence of ENSO on drought events. They used a combination of techniques including the SPEI (Meza 2013), return intervals of droughts based on L-moments under different precipitation thresholds (Núñez et al. 2011), and the long-term recurrence rate of extreme drought events calculated from tree-ring-based reconstructions of aridity indices (Christie et al. 2011). We applied the peak over threshold (POT) approach to study drought recurrence using thresholds of ≤40th percentile (P40) and ≤30th percentile (P30) for moderate, ≤20th percentile (P20) for severe, and ≤10th percentile (P10) for extreme drought events calculated over both subregional series. In addition, we searched for consecutive drought events of 2–4 years using the same percentile thresholds indicated above. For estimating the recurrence rate of drought events, we used a kernel estimation technique with a Gaussian function and 20-yr bandwidth. The kernel-based estimation of drought recurrence allows for detection of nonlinear and nonmonotonic trends without imposing parametric restrictions. Furthermore, a smooth kernel function produces more realistic estimation of drought recurrence. We calculated a confidence interval at the 95% level based on 1000 bootstrap resampling steps (Cowling et al. 1996) to estimate bias and variance properties of drought recurrence in MA. The kernel estimation, bandwidth selection, and bootstrap algorithm were computed in the free R Project platform software (R Core Team 2016).

3. Results

a. Spatial and temporal hydroclimatic variations

The PCA identifies dominant patterns of hydroclimate variability explaining a large percentage of the total variance of precipitation (72.5%), streamflow (84%), and snowpack (64.6%) across the MA. Smaller percentages of the variance are explained by PC2 and the third principal component (8.9% and 5.4% for precipitation, 5.7% and 4.8% for streamflow, and 11.6% and 9% for snowpack, respectively). Similar results were obtained using the mean streamflow for warm season months (October–February; PC1 = 86.1% and PC2 = 6.1%) and using total winter precipitation (May–September; PC1 = 74% and PC2 = 10%). Based on these results, we determined two spatiotemporal modes for the hydroclimate of the MA, the northern and southern subregions (Fig. 2). The northern hydroclimatic subregion is characterized by precipitation, streamflow, and snowpack stations located between 30° and 33°S (Figs. 2a–d). The southern subregional modes are represented by the PC2 of precipitation, PC1 of streamflow, and PC1 of snowpack, with the largest loadings of precipitation located between 34.5° and 37°S (Fig. 2e), from 34° to 35°S for the streamflow (Fig. 2f), and from 34° to 36°S for the snowpack (Fig. 2g). We are considering the PC modes of streamflow, snowpack, and precipitation, represented by the PC1 of streamflow, PC1 of snowpack, and PC2 of precipitation, with a significant mean correlation among them ($r = 0.70$; $P < 0.001$; Fig. 2h). The hydroclimate of the MA shows a north–south latitudinal gradient characterized by a marked interannual pattern in the northern subregion represented by the PC1 of precipitation, the PC2 of streamflow, and the PC2 of snowpack, with a strong correlation between them (mean $r = 0.69$; $P < 0.001$).

b. Interannual and decadal relationships between hydroclimate variations and large-scale climate forcings

The hydroclimatic variables from the northern subregion show significant correlations with the May–August Niño-3.4 index over the common period. Precipitation PC1 shows the largest correlation coefficient (1960–2000 period; $r = 0.55$; $P < 0.001$), followed by streamflow PC2 (1954–2007 period; $r = 0.53$; $P < 0.001$) and snowpack PC2 (1961–90 period; $r = 0.44$; $P < 0.05$; Fig. 3a). For the southern subregion, only the snowpack PC1 shows a significant correlation with the Niño-3.4 index between May and August ($r = 0.51$; $P < 0.01$; Fig. 3b).

The decadal to multidecadal PDO and IPO climate forcings show significant relationships with streamflow PC2 ($r = 0.31$; $P < 0.05$) and snowpack PC2 from the northern subregion ($r = 0.44$; $P < 0.05$; Fig. 3c), while for the southern subregion statistically significant relationships are found with streamflow PC1 ($r = 0.45$; $P < 0.05$) and precipitation PC2 ($r = 0.31$; $P < 0.05$; Fig. 3d). Relationships between the IPO and the hydroclimatic variables are significantly correlated only with streamflow PC2 in the northern subregion ($r = 0.38$; $P < 0.05$; Fig. 3e). On the contrary, the relationships with the IPO are significant with streamflow PC1 ($r = 0.33$; $P < 0.05$), precipitation PC2 ($r = 0.45$; $P < 0.05$), and snowpack PC1 ($r = 0.43$; $P < 0.05$; Fig. 3f).

The northern and southern subregional hydroclimatic patterns identified by PCA are shown in Fig. 4a. This time series (1910–2011) was constructed using the means of the precipitation, streamflow, and snowpack stations summarized in Table A1 of the appendix given loading factors ≥0.70 for each PCA. Larger-amplitude variability is observed in the northern subregion compared to the southern subregion, mainly between the 1940s and

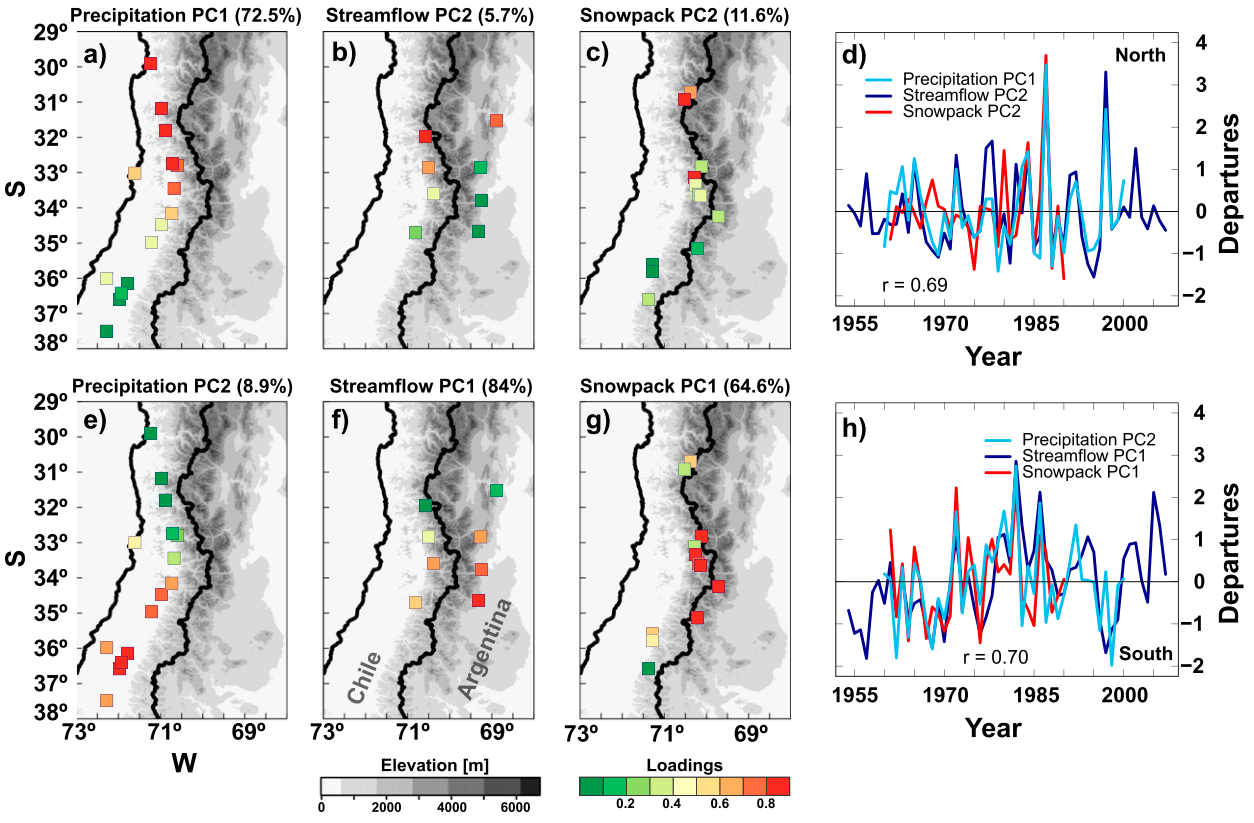

FIG. 2. The factor loadings (eigenvectors) for PC1 and PC2 of (a),(e) the annual precipitation (January–December) stations network; (b),(f) the annual streamflow (July–June) stations network; and (c),(g) the snowpack stations. The PCA of the precipitation stations was calculated over their 1960–2000 common period, the streamflow stations during the 1954–2007 common period, and snowpack stations between 1961 and 1990. The colors represent the loading factor values for the first two PCs of precipitation, streamflow, and snowpack. The percentage (%) of variance explained by each specific component is indicates in parentheses. Also shown is the comparison between the temporal amplitudes of the (d) "northern" and (h) "southern" streamflow, precipitation, and snowpack PCs. Mean Pearson correlation values between the PC amplitudes of streamflow, precipitation, and snowpack are indicated for the 1961–90 period (significant at $P < 0.001$).

1985–2010 (Figs. 4b,c). In addition to these differences, monthly precipitation amounts are around 3 times larger in the southern subregion compared to the northern part of the MA (Fig. 4d).

When the northern and southern subregional hydroclimatic patterns are compared in terms of the Pearson correlation with the Niño-3.4 SST index using 16-yr running blocks, significant correlation coefficients and periods are found throughout the twentieth century in the northern subregion. A similar pattern is obtained between the southern subregion and ENSO. However, nonsignificant coefficients between 1948 and 1975 are observed when considering temporal changes in the mean using the Mann–Whitney test (Fig. 5a). The influence of ENSO is generally present in the MA. However, our results demonstrate that the ENSO influence seems to be slightly stronger over the northern subregion. The northern and southern subregional series show coherence with positive/negative phases of PDO during 1910–2011. Furthermore, the Pearson correlation analysis between the PDO and both hydroclimatic subregion time series shows similar correlation coefficients for the 1910–2011 period (Fig. 5b). As with the PDO relationships, coherence between the northern and southern hydroclimatic subregions and negative/positive phases of IPO are observed over the 1910–2007 period. The IPO index shows significant correlation with the northern subregion over the 1932–50 and 1985–2000 periods, using 16-yr running blocks. However, a greater correlation between IPO and the southern subregion is present beginning in the 1970s (Fig. 5c). Despite this, the decadal and multidecadal variability related to the PDO and IPO shows general nonsignificant relationships over the analyzed period.

c. *Drought recurrence over the Mediterranean Andes*

Recurrence intervals of moderate to extreme drought events show different patterns in both subregions across the twentieth century. The northern subregion shows drought recurrences between ~2 and 4 years—droughts approximately every 2–4 years—during the 1910–25

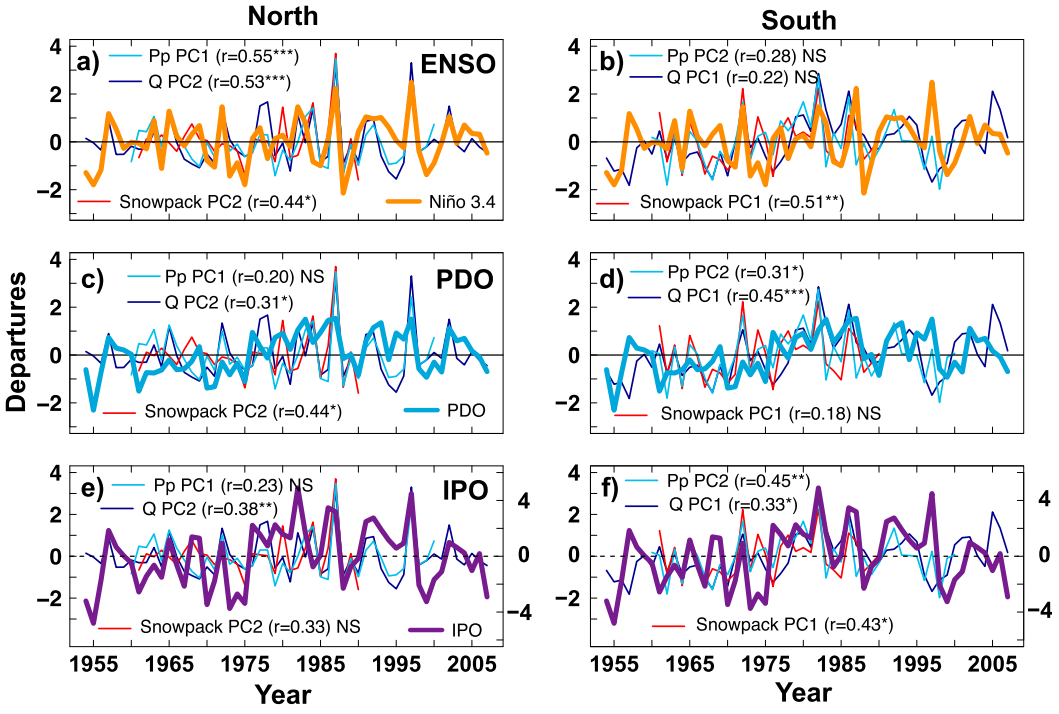

FIG. 3. (left) Factor scores of the PC2 of the annual (July–June) streamflow series, the PC1 of the annual (January–December) precipitation series, and the PC2 of the snowpack contrasted to (a) the winter (May–August) Niño-3.4 SST, (c) the annual (July–June) PDO index, and (e) the annual (July–June) IPO index. (right) Factor scores of the PC1 of the annual (July–June) streamflow series, the PC2 of the annual (January–December) precipitation series, and the PC1 of the snowpack contrasted to (b) the winter (May–August) Niño-3.4 SST, (d) the annual (July–June) PDO index, and (f) the annual (July–June) IPO index. The factor scores are grouped as northern and southern subregions inferred from the PCA summarized in Fig. 2. Significance levels are indicated, where one asterisk = $P < 0.05$, two asterisks = $P < 0.01$, three asterisks = $P < 0.001$, and NS = not significant.

period using the P40 threshold (moderate drought). Since the 1930s, an increase in drought recurrence is observed, reaching its highest recurrence peak of ~1.8 years between 1960 and 1970 and a drought recurrence of ~2–3 years during the 1980s (Fig. 6a). The southern hydroclimatic subregion shows a similar pattern from 1910 to 1925 and a sharp increase in drought recurrence during the 1930–55 period, with recurrence intervals decreasing from ~10 to 1.7 years and a high concentration of droughts between 1945 and 1975. Drought recurrences of 3 and ~2 years are seen between 1980 and 2011 in the southern subregion (Fig. 6b). In addition, three notable stages with different drought recurrence values are observed for the 1910–25, 1930–80, and 1981–2011 periods. The drought recurrence in the northern subregion based on P30 shows a recurrence interval of ~10 years between 1910 and 1935 with an increase in drought recurrence toward the 1970s, taking intervals of 2–3 years of recurrence in 2011 (Fig. 6c). Results similar to P40 are seen in the southern subregion using the P30 threshold (Fig. 6d).

Drought recurrence based on P20 (severe drought) shows an increase between 1940 and 1970 in both hydroclimatic subregions (Figs. 6e,f). A decreasing trend observed in the northern subregion since the 1990s can be contrasted with an increase in the drought recurrence in the southern subregion, particularly in the last decade.

Drought recurrence below the P10 threshold—extreme droughts—are recorded in the northern and southern subregions between 1910 and 1950 (Figs. 6g,h). An increase in drought recurrence in the northern subregion is observed over the 1950–90 interval with the highest recurrence peak of ~4 years, which continues with a decreasing trend toward the year 2011 with a recurrence of ~8 years. An increase in recurrence interval is observed in the southern subregion between 1950 and 1970, with the highest recurrence peak of ~4 years in the 1960s. Since the year 1985, a positive trend in drought recurrence is observed toward the year 2011 (Fig. 6h). Independent of the percentile threshold used, a concentration of dry extremes has been recorded in both regions since the 1950s, showing that the first half of the twentieth century was wetter than the second half for the MA.

The recurrence of consecutive 2-yr droughts using the P40 threshold shows an increase in the northern and

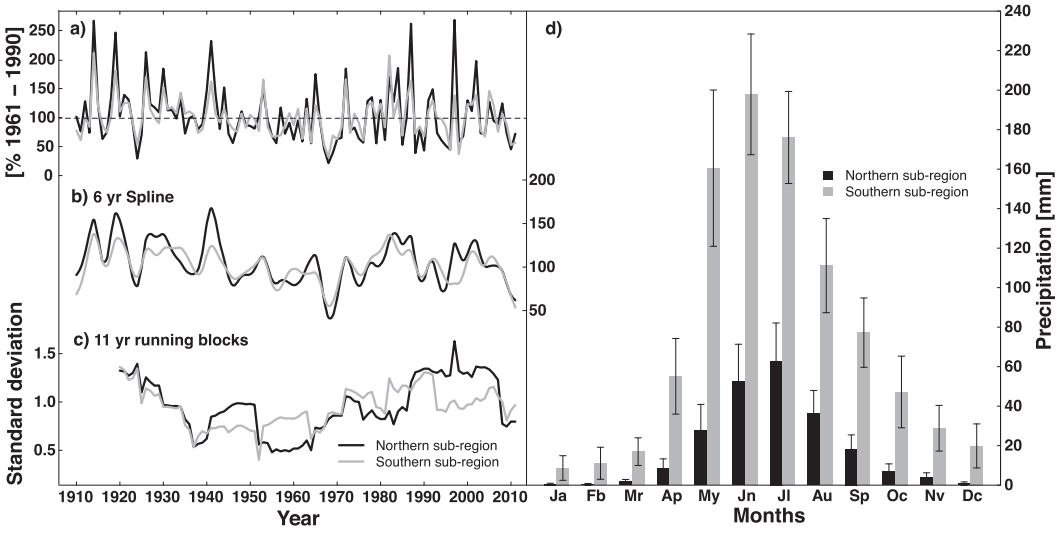

FIG. 4. (a) The northern and southern subregional hydroclimatic series integrating streamflow, precipitation, and snowpack identified by the PCA aggregate. The selected stations are summarized in Table A1. Both time series span the 1910–2011 period. The horizontal dashed line represents the regional mean value (100%) based on the years 1961–90 of the common analysis period. (b) As in (a), but for a time series with a 6-yr cubic spline filter to show the amplitude patterns. The units of the *y* axis values represent the amplitude. (c) As in (a), but for a time series with an 11-yr moving std dev to highlight temporal variations in both hydroclimatic subregions. (d) Monthly precipitation distribution (mm) of the northern and southern subregions. Precipitation stations summarized in Table A1 have been chosen to calculate monthly amounts. The error bars represent plus/minus one monthly std dev. The mean monthly precipitation was calculated over the 1963–2000 period.

southern subregion since the 1970s with a recurrence interval of ~7 years in 2011 (Fig. 7a). In the case of consecutive 3-yr drought events, an increase is observed since the 1930s in both subregions (Fig. 7b), with a decline in recurrence of 3-yr droughts in the southern subregion around the 1980s until the present. A similar result is observed using consecutive 4-yr drought events, but the northern subregion shows no trend since the 1980s (Fig. 7c). Similar trends to the P40 were found for drought events using the P30 threshold, indicating an increase in the recurrence interval since the 1910s in the northern subregion and since the 1980s in the southern subregion using consecutive 2-yr droughts (Fig. 7d), reaching the highest recurrence (~10 years) during the last decade. The consecutive 3-yr drought events using the P30 threshold show a similar pattern to consecutive 4-yr droughts using the P40 threshold (Fig. 7e). Consecutive 4-yr droughts using the P30 threshold are observed only in the northern subregion, with the highest recurrence peak occurring during the 1970s (Fig. 7f). The 2-yr drought recurrence using the P20 threshold—severe droughts—in both subregions seem to increase from an average recurrence of ~50 years prior to the 1970s and close to ~20 years after the 1970s (Fig. 7g). Similar results are obtained using consecutive 3-yr droughts, but these events are less recurrent since the 1980s in the southern subregion (Fig. 7h). The recurrence of consecutive 2-yr droughts using the P10 threshold (extreme drought) has been increasing since the 1960s in both subregions (Fig. 7i). Extreme and consecutive 3-yr drought events are registered only in the northern subregion around the 1960s, with the highest recurrence peak during the 1970s (Fig. 7j).

4. Discussion

The present study identifies the spatial and temporal patterns in the hydroclimate across the MA, where, despite a general common pattern across the region, which encompasses a strong north–south annual precipitation gradient from 247.6 to 1070.4 mm, two distinct hydroclimatic subregions have been identified based upon PCA. The results show that the northern subregion (30°–34°S) exhibits an interannual mode of variability represented by precipitation PC1, streamflow PC2, and snowpack PC2 (Fig. 2d), while a mode with lower amplitude has been obtained in the southern subregion from precipitation PC2, streamflow PC1, and snowpack PC1 (Fig. 2h). Differences in the location of the PC modes of variability between variables could be associated with 1) a longer latitudinal range (29°–38°S) of precipitation stations than the streamflow and snowpack records, 2) the geographical concentration of streamflow and snowpack measurements (31.5°–35° and 31°–37°S), and 3) proximity of the streamflow and snowpack stations to the 33.5°–34°S

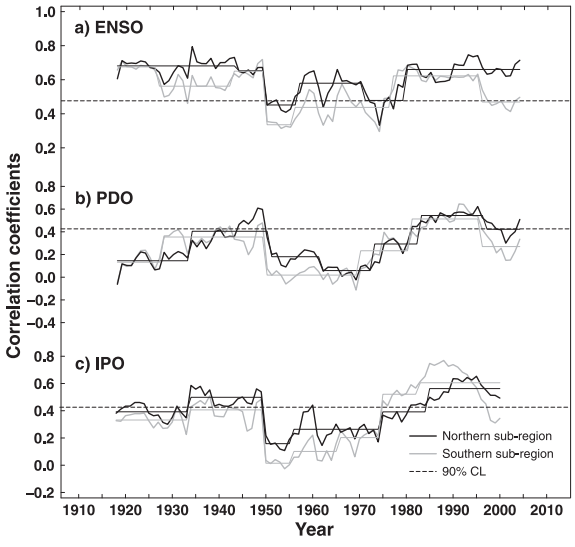

FIG. 5. (a) Correlation coefficients between the northern and southern subregional hydroclimatic series and the winter (May–August) Niño-3.4 SST using a 16-yr running block. (b) Correlation coefficients between the northern and southern subregional hydroclimatic series and the July–June PDO index using a 16-yr running block. (c) As in (b), but for the July–June IPO index using a 16-yr running block. The horizontal dashed lines indicate statistical confidence of Pearson correlations (critical $r = \pm 0.425$; $P < 0.10$ using two-tailed test). Moving Pearson correlation has been calculated using the northern and southern subregion series expressed by standardized anomalies (Z values) using 1910–2007 as the reference period given by the IPO index register. Horizontal lines in the time series represent temporal and significant mean correlation shifts at $P < 0.05$ using the Mann–Whitney test.

latitudinal. However, the similar patterns identified between PC modes of hydroclimatic variables analyzed could be related to the same source of humidity that comes from the Pacific Ocean as frontal systems.

During recent decades, the northern subregion pattern has exhibited higher interannual variability than the southern pattern. However, this is not a stationary feature, and it highlights the complex temporal dimension of hydroclimate across the precipitation gradient of the MA (Figs. 4a–d). This finding has been observed by Garreaud et al. (2009), who describe that year-to-year fluctuations in precipitation over the MA can be up to one-third of its annual mean, uniting the MA with northeastern Brazil, the northern coast of Peru, and southern Argentina as the region of South America with the highest level of interannual variability. The northern subregion of the MA shows much smaller monthly precipitation amounts compared to the southern subregion (Fig. 4d). In addition, this subregion also exhibits a significant relationship with winter Niño-3.4 SST of ENSO variability during the last century (Fig. 5a). Under normal conditions, the monthly average precipitation is low in the northern subregion and can be extremely low during dry La Niña episodes of ENSO. This result could help to distinguish a northern subregion with high interannual variability that is more vulnerable during dry episodes. Also, this result could help to clarify regional effects of climate change on society (i.e., social conflicts for water resources and lack of freshwater), where future projections based on regional climate models indicate precipitation reductions over the whole MA (CONAMA 2006).

Although an ENSO influence is recorded in both subregions of the MA, the influence seems to be slightly stronger north of 34°S but nonstationary across the twentieth century (Fig. 5a). This relationship between ENSO and the hydroclimate in the northern subregion is congruent with previous studies relating ENSO with precipitation over central Chile (Escobar and Aceituno 1998; Montecinos and Aceituno 2003; Garreaud et al. 2009), with streamflow variability in Chile (Aceituno and Vidal 1990; Aceituno and Garreaud 1995; Muñoz et al. 2016) and Argentina (Compagnucci et al. 2000), and with snowpack accumulation in the central Andes (Masiokas et al. 2006). In particular, the relationship between ENSO in the northern subregion and precipitation could explain the positive trend between 1975 and 2000 reported in several studies (Carrasco et al. 2005; Quintana and Aceituno 2012). Furthermore, warm El Niño events are among the most important modulators of streamflow center timing variations in the northern subregion (Cortés et al. 2011). Based on PCA results and correlation values presented in this study, ENSO would be the main controller of hydroclimatic variability across 30°–37°S in interannual scales.

Long-term climate forcings such as the PDO and IPO show similar variation in both subregions across the twentieth century (Figs. 5b,c). However, a greater relationship has been found between IPO and the southern pattern and observed since the mid-1970s (Fig. 5c). The significant correlation coefficients between the MA hydroclimate and IPO could be associated with the 1976–77 cold-to-warm SST shift in the tropical Pacific Ocean, well documented in South America by Jacques-Coper and Garreaud (2015). In addition, we also think that this could explain the results obtained between the individual PCs and the IPO and PDO, where a smaller but significant correlation has been obtained (see Fig. 3). However, despite generally nonsignificant relationships observed for the MA hydroclimate and the IPO and PDO over the twentieth century, the temporal hydroclimate variability in both subregions seems to be modulated by decadal to multidecadal teleconnection mechanisms from the Pacific Ocean. We hypothesize that these mechanisms could explain the long-term similitudes observed in the time series from both

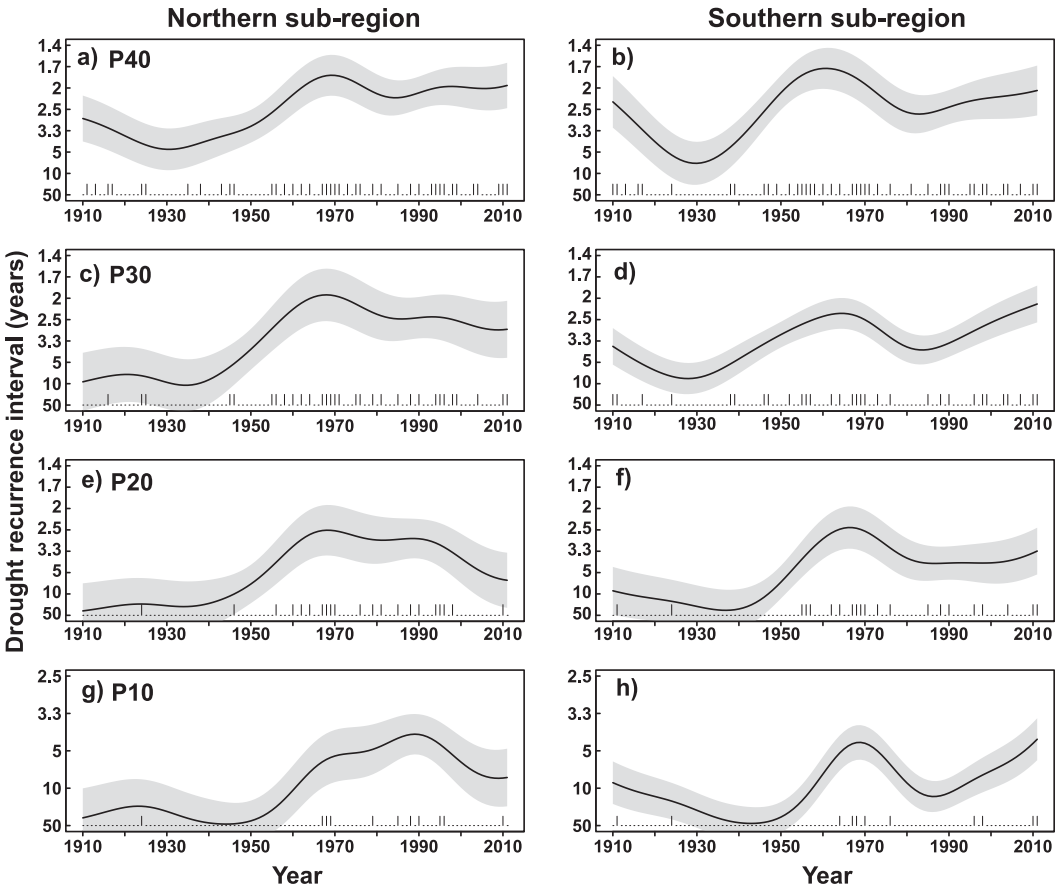

FIG. 6. Recurrence intervals (years; solid black line) of extreme drought events calculated for the northern and southern hydroclimatic subregions based on cumulative magnitude of dry years using percentile threshold values (a),(b) P40; (c),(d) P30; (e),(f) P20; and (g),(h) P10, calculated with kernel estimation using a bandwidth of 20 years. The gray shading represents the 95% confidence interval based on 1000 bootstrap simulations. The dry event years based on the respective percentile threshold are indicated at the bottom of each solid line.

subregions. Nevertheless, future studies should focus on untangling the relationships between the IPO and PDO and individual hydroclimatic variables (i.e., precipitation). This could be crucial to understanding long-term teleconnection processes over the MA. Similar signatures of decadal to multidecadal teleconnection mechanisms have been found in others regions of the world, such as the western United States (McCabe and Dettinger 1999) and around the globe (McCabe and Palecki 2006).

Some discrepancies in the relationships between these climate forcings and the modes of variability obtained from the PCA have been observed throughout the last half century. Regional snowpack (PC2) for the northern subregion shows a significant correlation with the PDO. We speculate that these results could be influenced by the positive wet phase of the PDO, jointly occurring with severe El Niño events that occurred between 1976 and 1990, with higher-than-normal snow accumulation and river discharges found across the MA over this period. Low correlation values obtained between the PDO and snowpack PC1 in the southern subregion could be explained by the fact that the annual precipitation regime (strongly correlated with snowpack accumulation) is influenced by other climatic factors such as the South Pacific subtropical anticyclone (SPSA) latitudinal position (Aceituno 1988; Montecinos and Aceituno 2003). The SPSA is the main controller of moisture-rich airflow in the winter season (Montecinos et al. 2011). Furthermore, snowpack accumulation and persistence are related to other physical processes such as the energy balance between snow surface and the atmosphere, controlled by net shortwave radiation and air temperature, variables not quantified in this work. Multidecadal variations such as the IPO show a significant correlation with snowpack PC1 in the southern hydroclimatic subregion. Snowpack PC1 and precipitation PC2 seem to be better

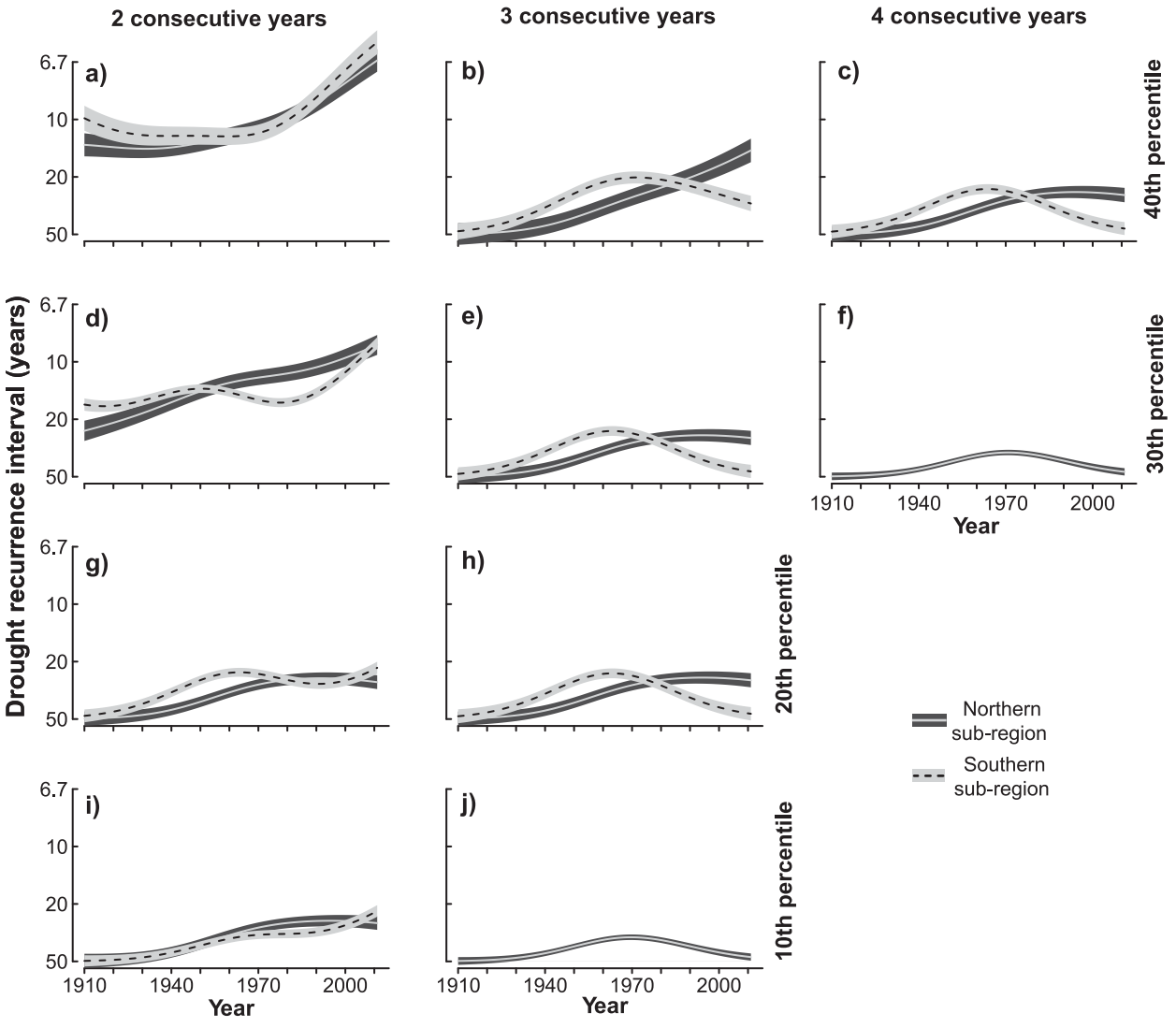

FIG. 7. (a)–(j) Consecutive drought recurrence intervals running for 2–4 years calculated by the northern and southern subregion using the P10–P40 percentile threshold. A bandwidth of 20 years has been chosen in all cases to estimate the recurrence. The confidence bands at 95% have been obtained from 1000 bootstrap simulations.

connected with this climate forcing in the analyzed period (Fig. 3f). Similar results are obtained using moving correlations with 16-yr running blocks between the IPO and the southern pattern, with an increase in correlation coefficients between 1975 and 2000 (Fig. 5c).

Drought recurrence shows temporal variation in both subregions across the twentieth century (Figs. 6, 7). However, drought recurrence analysis using different thresholds shows that the first half of the twentieth century was wet in both subregions, in contrast to the second half, which was characterized by dry conditions (Fig. 6). On the other hand, both subregions show an increase in drought recurrence between 1945 and 1975. However, an increase in drought recurrence after 1975 is observed mainly in the southern subregion. Consecutive and moderate drought recurrence every 2 years shows an increase since the 1970s in both subregions. Furthermore, decadal to multidecadal variations produced by the PDO and the IPO show increased correlations in both subregions since 1975 (Figs. 5b,c).

Mantua and Hare (2002) have identified a ''cool'' PDO regime that prevailed in the 1947–76 period, while ''warm'' PDO regimes dominated from 1925 to 1946 and from 1977 to the mid-1990s. In addition, Masiokas et al. (2010) documented coherence between both phases of the PDO with snowpack and river discharge in the same geographical region. Similarly,

Rubio-Álvarez and McPhee (2010) found significant temporal relationships between PDO activity and winter streamflow (April–September) using gauge stations from 35.5° to 36.5°S. The negative phase of the PDO and IPO (i.e., 1945–75 period) would explain extreme dry phases registered in the last century (i.e., 1960–70; Figs. 6g,h).

Consecutive 2-yr drought recurrence intervals show similar variability in both subregions when the PDO and IPO phase shifts have occurred. The different drought recurrence trends observed in both subregions between 2000 and 2011 (negative in the northern and positive in the southern subregion; Figs. 6e–h) could be related to interannual variability. For instance, the Oceanic Niño Index (ONI) of ENSO reports four El Niño and La Niña events with weak to moderate magnitudes registered over the same period. Interestingly, the last half of the twentieth century has been dominated by El Niño–like conditions, which are normally associated with moist years in the MA. However, ENSO activity explains only around one-third of the interannual variability of precipitation in the MA (Montecinos and Aceituno 2003). We hypothesize that high-latitude climate forcings created by the southern annular mode (SAM)—also called the Antarctic Oscillation (AAO)—could be an alternative explanation to the increasing drought recurrence in the MA registered in the last half of the twentieth century and between 2000 and 2011. The AAO shows a positive trend in activity since the 1950s that is unprecedented in the last six centuries (Villalba et al. 2012). In addition, the persistence of dry conditions since the 1980s observed in the southern subregion could be associated with the strong reduction of precipitation observed in instrumental records and forced by a southward shift and intensification of the SPSA (Quintana and Aceituno 2012).

Drought recurrence intervals reported in this study are congruent with previous estimates of drought return period estimations in northern and central Chile (Núñez et al. 2011). These authors evaluated drought recurrence based on precipitation reduction rates, where reductions below 40% of normal in the northern subregion (north of ~32°S) produced drought return periods of ~3–4 and 10 years around 33°S. In central southern Chile (south of ~34°S), these reductions produced return periods of 22 years. In addition, Núñez et al. (2011) showed a similar north–south transition between 32.5° and 34°S for drought return periods from interannual to decadal interval values, respectively. This result supports the spatial distribution of loading factors obtained from the PCA and the division of the MA into two subregions performed in this study (Fig. 2).

Future research should aim at refining global and regional climate models in order to integrate variables such as ENSO and to better understand the interaction between the MA hydroclimate and decadal to multidecadal mechanisms from the Pacific Ocean. These points could be relevant in order to estimate availability of water in the MA under future climate scenarios. In a region of South America where drought has resulted in significant economic and social impacts, future drought assessments are especially relevant to adaptation strategies and water management policies.

5. Conclusions

In this study we evaluated the spatiotemporal variations of hydroclimatic variables and regional drought recurrence in the Mediterranean Andes since the early twentieth century (1910–2011 period), using high-quality instrumental records of snowpack, precipitation, and streamflow. Despite the identification of a general common pattern, the MA climate and factors impacting it are best understood as two hydroclimatic subregions, with a latitudinal hydroclimatic transition between 33° and 34°S. The northern subregion shows greater interannual variability associated with ENSO activity when compared with the southern subregion, which leads to a higher vulnerability of water resources in the northern subregion under dry intervals. However, the decadal to multidecadal teleconnections associated with the PDO and IPO are observed across the entire MA. In spite of this, the relationships between the MA hydroclimate and these decadal SST patterns were generally nonsignificant across the twentieth century. However, since the mid-1970s, variations induced by the IPO were significant and greater in the southern subregion in contrast to the northern subregion. The use of such teleconnections for hydroclimate prediction should be used with caution and will likely need to account for their varying strength, recognizing that they may not always provide a strong enough signal to be useful in characterizing regional hydroclimates (i.e., Boisier et al. 2016). Understanding the underlying dynamics leading to these changes relationships remains a critical climate science need.

Drought recurrence periods show different patterns between the two hydroclimatic subregions, especially since the 1980s. Persistent drought conditions are observed in the northern subregion since the 1950s, with a peak during the 1970s. Likewise, the southern subregion exhibits a majority of years under dry conditions, with increased recurrence intervals since the 1980s. However, both subregions show more drought events since the second half of the twentieth century. We believe that the information reported in the present work is relevant for a better understanding of hydroclimatic variability, water resources

TABLE A1. Summary of loading factors for PC1 and PC2 derived from the PCA of the snowpack, precipitation, and streamflow records of the MA utilized. Station loadings in boldface (values ≥0.70) have been used to construct two hydroclimatic subregional series covering the 1910–2011 period. CL and AR indicate Chile and Argentina, respectively.

Station register	Stations (country)	PC1	PC2
Snowpack	QLA (CL)	0.27	**0.81**
	CVN (CL)	0.31	**0.88**
	POR (CL)	**0.74**	0.34
	CNE (CL)	0.36	**0.84**
	BNE (CL)	**0.82**	0.46
	LNE (CL)	**0.84**	0.40
	LDI (AR)	**0.86**	0.36
	VHE (AR)	**0.83**	0.18
Precipitation	LSE (CL)	**0.85**	0.27
	COM (CL)	**0.89**	0.32
	SAL (CL)	**0.90**	0.32
	SFP (CL)	**0.90**	0.33
	LAN (CL)	**0.83**	0.44
	QUI (CL)	**0.81**	0.48
	SFE (CL)	0.54	**0.75**
	CUR (CL)	0.54	**0.75**
	CAU (CL)	0.54	**0.71**
	PAR (CL)	0.25	**0.84**
	SCA (CL)	0.35	**0.81**
	CHI (CL)	0.22	**0.83**
	LAG (CL)	0.25	**0.71**
Streamflow	SJU (AR)	0.48	**0.83**
	CHO (CL)	0.40	**0.90**
	ACO (CL)	0.61	**0.76**
	MZA (AR)	**0.76**	0.47
	MAI (CL)	**0.75**	0.61
	TUN (AR)	**0.82**	0.42
	DIA (AR)	**0.89**	0.38
	TIN (CL)	**0.70**	0.52

planning, and vulnerability in the MA and demonstrates the need for future studies focused on better understanding the MA area as two hydroclimatic subregions.

Acknowledgments. This research was supported by Fondo Nacional de Desarrollo Científico y Tecnológico (FONDECYT) project 1121106. Álvaro González-Reyes wishes to thank Comisión Nacional de Investigación Científica y Tecnológica–Programa de Capital Humano Avanzado (CONICYT-PCHA)/Doctorado Nacional/2016-21160642 for the doctoral scholarship. We acknowledge support from Fondo de Financiamiento de Centros de Investigación en Áreas Prioritarias (FONDAP) 15110009 [Center for Climate and Resilience Research (CR)2] and Dirección de Investigación y Desarrollo (DID), Universidad Austral de Chile. Sebastian Crespo and Ariel Muñoz acknowledge support from Vicerrectoría de Investigación y Estudios Avanzados–Pontificia Universidad Católica de Valparaíso (VRIEA-PUCV) 039.353/2016. We thank the three anonymous reviewers and the editors that contributed to improving this paper.

APPENDIX

Loading Factors Summary

Table A1 summarizes the loading factors obtained from the PCA by each hydroclimatic station of snowpack, precipitation, and streamflow records of the MA region.

REFERENCES

Aceituno, P., 1988: On the functioning of Southern Oscillation in the South American sector. Part I: Surface climate. *Mon. Wea. Rev.*, **116**, 505–524, doi:10.1175/1520-0493(1988)116<0505:OTFOTS>2.0.CO;2.

——, and F. Vidal, 1990: Variabilidad en el caudal interanual en ríos andinos en Chile central en relación con la temperatura de la superficie del mar en el Pacífico central. *Rev. Soc. Chil. Ing. Hidraul.*, **5**, 7–19.

——, and R. Garreaud, 1995: Impactos de los fenómenos El Niño y La Niña en regímenes fluviométricos andinos. *Rev. Soc. Chil. Ing. Hidraul.*, **10**, 33–43.

Boisier, J. P., R. Rondanelli, R. D. Garreaud, and F. Muñoz, 2016: Anthropogenic and natural contributions to the southeast Pacific precipitation decline and recent megadrought in central Chile. *Geophys. Res. Lett.*, **43**, 413–421, doi:10.1002/2015GL067265.

Bown, F., A. Rivera, and C. Acuña, 2008: Recent glacier variations at the Aconcagua basin, central Chilean Andes. *Ann. Glaciol.*, **48**, 43–48, doi:10.3189/172756408784700572.

Carrasco, J. F., G. Casassa, and J. Quintana, 2005: Changes of the 0°C isotherm and the equilibrium line altitude in central Chile during the last quarter of the 20th century. *Hydrol. Sci. J.*, **50**, 933–948, doi:10.1623/hysj.2005.50.6.933.

——, R. Osorio, and G. Casassa, 2008: Secular trend of the equilibrium-line altitude on the western side of the southern Andes, derived from radiosonde and surface observations. *J. Glaciol.*, **54**, 538–550, doi:10.3189/002214308785837002.

Christie, D. A., and Coauthors, 2011: Aridity changes in the temperate–Mediterranean transition of the Andes since AD 1346 reconstructed from tree-rings. *Climate Dyn.*, **36**, 1505–1521, doi:10.1007/s00382-009-0723-4.

Compagnucci, R. H., and Coauthors, 2000: Variability in subtropical Andean Argentinean Atuel River; A wavelet approach. *Environmetrics*, **11**, 251–269, doi:10.1002/(SICI)1099-095X(200005/06)11:3<251::AID-ENV405>3.0.CO;2-0.

CONAMA, 2006: Climate variability in Chile in the XXI century (in Spanish). Corporación Nacional del Medio Ambiente, accessed 8 August 2016. [Available online at http://dgf.uchile.cl/PRECIS/.]

Cortés, G., X. Vargas, and J. McPhee, 2011: Climatic sensitivity of streamflow timing in the extra tropical western Andes Cordillera. *J. Hydrol.*, **405**, 93–109, doi:10.1016/j.jhydrol.2011.05.013.

Cowling, A., P. Hall, and M. j. Phillips, 1996: Bootstrap confidence regions for the intensity of a Poisson point process. *J. Amer. Stat. Assoc.*, **91**, 1516–1524, doi:10.1080/01621459.1996.10476719.

CR2, 2016: The state of drought in Chile this 2016 (in Spanish). Centro de Clima y de Resiliencia, accessed 11 August 2016. [Available online at http://www.cr2.cl/estado-de-la-sequia-2016-en-chile-por-rene-garreaud/.]

Escobar, F., and P. Aceituno, 1998: ENSO influence on Andean winter snowfall in central Chile (in Spanish). *Bull. Inst. Fr. Études Andines*, **27** (3), 753–759.

Falvey, M., and R. Garreaud, 2009: Regional cooling in a warming world: Recent temperature trends in the southeast Pacific and along the west coast of subtropical South America (1979–2006). *J. Geophys. Res.*, **114**, 1–16, doi:10.1029/2008JD010519.

Garreaud, R., 2009: The Andes climate and weather. *Adv. Geosci.*, **22**, 3–11.

——, M. Vuille, R. Compagnucci, and J. Marengo, 2009: Present day South American climate. *Palaeogeogr., Palaeoclimatol., Palaeoecol.*, **281**, 180–195, doi:10.1016/j.palaeo.2007.10.032.

INDEC, 2010: National census, 2010. Instituto Nacional de Estadística y Censos, accessed 9 January 2016. [Available online at http://www.indec.gob.ar/nivel4_default.asp?id_tema_1=2&id_tema_2=41&id_tema_3=135.]

INE, 2003: National census, 2002 (in Spanish). Instituto Nacional de Estadísticas, accessed 9 January 2016. [Available online at http://www.ine.cl/cd2002/sintesiscensal.pdf.]

Jacques-Coper, M., and R. Garreaud, 2015: Characterization of the 1970s climate shift in South America. *Int. J. Climatol.*, **35**, 2164–2179, doi:10.1002/joc.4120.

Le Quesne, C., C. Acuña, J. Boninsegna, A. Rivera, and J. Barichivich, 2009: Long-term glacier variations in the central Andes of Argentina and Chile, inferred from historical records and tree ring reconstructed precipitation. *Palaeogeogr., Palaeoclimatol., Palaeoecol.*, **281**, 334–344, doi:10.1016/j.palaeo.2008.01.039.

Lliboutry, L., 1998: Glaciers of the dry Andes. Satellite Image Atlas of Glaciers of the World: South America, R. S. Williams and J. G. Ferrigno, Eds., USGS Professional Paper 1386-I. [Available online at http://pubs.usgs.gov/prof/p1386i/index.html.]

Mantua, N. J., and S. R. Hare, 2002: The Pacific decadal oscillation. *J. Oceanogr.*, **58**, 35–44, doi:10.1023/A:1015820616384.

——, ——, Y. Zhang, J. Wallace, and R. C. Francis, 1997: A Pacific interdecadal climate oscillation with impacts on salmon production. *Bull. Amer. Meteor. Soc.*, **78**, 1069–1079, doi:10.1175/1520-0477(1997)078<1069:APICOW>2.0.CO;2.

Masiokas, M. H., R. Villalba, B. H. Luckman, C. Le Quesne, and J. C. Aravena, 2006: Snowpack variations in the central Andes of Argentina and Chile, 1951–2005: Large-scale atmospheric influences and implications for water resources in the region. *J. Climate*, **19**, 6334–6352, doi:10.1175/JCLI3969.1.

——, A. Rivera, L. E. Espizua, R. Villalba, S. Delgado, and J. C. Aravena, 2009: Glacier fluctuations in extratropical South America during the past 1000 years. *Palaeogeogr., Palaeoclimatol., Palaeoecol.*, **281**, 242–268, doi:10.1016/j.palaeo.2009.08.006.

——, R. Villalba, B. H. Luckman, and S. Mauget, 2010: Intra- to multidecadal variations of snowpack and streamflow records in the Andes of Chile and Argentina between 30° and 37°S. *J. Hydrometeor.*, **11**, 822–831, doi:10.1175/2010JHM1191.1.

——, ——, ——, E. Montaña, E. Betman, D. A. Christie, C. Le Quesne, and S. Mauget, 2013: Recent and historic Andean snowpack and streamflow variations and vulnerability to water shortages in central-western Argentina. *Vulnerability of Water Resources to Climate*, Vol. 5, *Climate Vulnerability: Understanding and Addressing Threats to Essential Resources*, R. A. Pielke, Ed., Elsevier, 213–227, doi:10.1016/B978-0-12-384703-4.00522-0.

McCabe, G., and M. Dettinger, 1999: Decadal variations in the strength of ENSO teleconnections with precipitation in the western United States. *Int. J. Climatol.*, **19**, 1399–1410, doi:10.1002/(SICI)1097-0088(19991115)19:13<1399::AID-JOC457>3.0.CO;2-A.

——, and M. Palecki, 2006: Multidecadal climate variability of global lands and oceans. *Int. J. Climatol.*, **26**, 849–865, doi:10.1002/joc.1289.

Meza, F., 2013: Recent trends and ENSO influence on droughts in northern Chile: An application of the standardized precipitation evapotranspiration index. *Wea. Climate Extremes*, **1**, 51–58, doi:10.1016/j.wace.2013.07.002.

Miller, A., 1976: The climate of Chile. *Climates of Central and South America*, Vol. 12, *World Survey of Climatology*, W. Schwerdtfeger, Ed., Elsevier, 113–131.

Montecinos, A., and P. Aceituno, 2003: Seasonality of the ENSO-related rainfall variability in central Chile and associated circulation anomalies. *J. Climate*, **16**, 281–296, doi:10.1175/1520-0442(2003)016<0281:SOTERR>2.0.CO;2.

——, M. V. Kurgansk, C. Muñoz, and K. Takahashi, 2011: Non-ENSO interannual rainfall variability in central Chile during austral winter. *Theor. Appl. Climatol.*, **106**, 557–568, doi:10.1007/s00704-011-0457-1.

Muñoz, A., and Coauthors, 2016: Streamflow variability in the Chilean temperate–Mediterranean climate transition (35°S–42°S) during the last 400 years inferred from tree-ring records. *Climate Dyn.*, **47**, 4051–4066, doi:10.1007/s00382-016-3068-9.

Núñez, J. H., K. Verbist, J. R. Wallis, M. G. Schaefer, L. Morales, and W. M. Cornelis, 2011: Regional frequency analysis for mapping drought events in north-central Chile. *J. Hydrol.*, **405**, 352–366, doi:10.1016/j.jhydrol.2011.05.035.

Power, S., T. Casey, C. Folland, A. Colman, and V. Mehta, 1999: Inter-decadal modulation of the impact of ENSO on Australia. *Climate Dyn.*, **15**, 319–324, doi:10.1007/s003820050284.

Quintana, J. M., and P. Aceituno, 2012: Changes in the rainfall regime along the extratropical west coast of South America (Chile): 30°–43°S. *Atmósfera*, **25**, 1–22.

R Core Team, 2016: R: A language and environment for statistical computing. R Foundation for Statistical Computing, accessed 10 January 2017. [Available online at www.R-project.org.]

Rubio-Álvarez, E., and J. McPhee, 2010: Patterns of spatial and temporal variability in streamflow records in south central Chile in the period 1952–2003. *Water Resour. Res.*, **46**, W05514, doi:10.1029/2009WR007982.

Rutllant, J., and H. Fuenzalida, 1991: Synoptic aspects of the central Chile rainfall variability associated with the Southern Oscillation. *Int. J. Climatol.*, **11**, 63–76, doi:10.1002/joc.3370110105.

Trenberth, K. E., 1997: The definition of El Niño. *Bull. Amer. Meteor. Soc.*, **78**, 2771–2777, doi:10.1175/1520-0477(1997)078<2771:TDOENO>2.0.CO;2.

Vera, C., and Coauthors, 2006: Toward a unified view of the American monsoon systems. *J. Climate*, **19**, 4977–5000, doi:10.1175/JCLI3896.1.

Villalba, R., and Coauthors, 2012: Unusual Southern Hemisphere tree growth patterns induced by changes in the southern annular mode. *Nat. Geosci.*, **5**, 793–798, doi:10.1038/ngeo1613.

Vuille, M., and J. P. Milana, 2007: High-latitude forcing of regional aridification along the subtropical west coast of South America. *Geophys. Res. Lett.*, **34**, L23703, doi:10.1029/2007GL031899.

Wilks, D. S., 2011: *Statistical Methods in the Atmospheric Sciences.* 3rd ed. International Geophysics Series, Vol. 100, Academic Press, 676 pp.

Zhang, Y., J. M. Wallace, and D. S. Battisti, 1997: ENSO-like interdecadal variability: 1900–93. *J. Climate*, **10**, 1004–1020, doi:10.1175/1520-0442(1997)010<1004:ELIV>2.0.CO;2.